



**Time-Resolved Observation and Control of
Superexchange Interactions with Ultracold Atoms in
Optical Lattices**

S. Trotzky, *et al.*
Science **319**, 295 (2008);
DOI: 10.1126/science.1150841

***The following resources related to this article are available online at
www.sciencemag.org (this information is current as of February 28, 2008):***

Updated information and services, including high-resolution figures, can be found in the online version of this article at:

<http://www.sciencemag.org/cgi/content/full/319/5861/295>

Supporting Online Material can be found at:

<http://www.sciencemag.org/cgi/content/full/1150841/DC1>

A list of selected additional articles on the Science Web sites **related to this article** can be found at:

<http://www.sciencemag.org/cgi/content/full/319/5861/295#related-content>

This article **cites 36 articles**, 1 of which can be accessed for free:

<http://www.sciencemag.org/cgi/content/full/319/5861/295#otherarticles>

This article appears in the following **subject collections**:

Physics

<http://www.sciencemag.org/cgi/collection/physics>

Information about obtaining **reprints** of this article or about obtaining **permission to reproduce this article** in whole or in part can be found at:

<http://www.sciencemag.org/about/permissions.dtl>

Time-Resolved Observation and Control of Superexchange Interactions with Ultracold Atoms in Optical Lattices

S. Trotzky,^{1*} P. Cheinet,^{1*} S. Fölling,¹ M. Feld,^{1,2} U. Schnorrberger,¹ A. M. Rey,³ A. Polkovnikov,⁴ E. A. Demler,^{3,5} M. D. Lukin,^{3,5} I. Bloch^{1†}

Quantum mechanical superexchange interactions form the basis of quantum magnetism in strongly correlated electronic media. We report on the direct measurement of superexchange interactions with ultracold atoms in optical lattices. After preparing a spin-mixture of ultracold atoms in an antiferromagnetically ordered state, we measured coherent superexchange-mediated spin dynamics with coupling energies from 5 hertz up to 1 kilohertz. By dynamically modifying the potential bias between neighboring lattice sites, the magnitude and sign of the superexchange interaction can be controlled, thus allowing the system to be switched between antiferromagnetic and ferromagnetic spin interactions. We compare our findings to predictions of a two-site Bose-Hubbard model and find very good agreement, but are also able to identify corrections that can be explained by the inclusion of direct nearest-neighbor interactions.

Quantum spin systems on a lattice have served for decades as paradigms for condensed matter and statistical physics, elucidating fundamental properties of phase transitions and acting as models for the emergence of quantum magnetism in strongly correlated electronic media. In all these cases, the underlying systems rely on a spin-spin interaction between particles on neighboring lattice sites, such as in the Ising or Heisenberg model (1–3). As initially proposed for electrons by Dirac (4, 5) and Heisenberg (2, 6), effective spin-spin interactions can arise due to the interplay between the spin-independent Coulomb repulsion and exchange symmetry and do not require any direct coupling between the spins of the particles. The nature of such spin-exchange interactions is typically short-ranged, as it is governed by the wave function overlap of the underlying electronic orbitals. However, in several topical insulators, such as ionic solids like CuO and MnO, antiferromagnetic order arises even though the wave function overlap between the magnetic ions is practically zero. In this case, a “superexchange” interaction mediated by higher-order virtual hopping processes can be effective over a large distance (7, 8), which leads to an (anti-)ferromagnetic coupling between bosons (fermions) on neighboring lattice sites (3). Such superexchange inter-

actions are believed to play an important role in the context of high-temperature superconductivity (9). Furthermore, they can form the basis for the generation of robust quantum gates similar to that recently described in electronic double quantum dot systems (10, 11) and can be used for the efficient generation of multiparticle entangled states (12, 13), as well as for the production of many-body quantum phases with topological order (14–16).

We report on the direct observation of superexchange interactions with ultracold atoms in optical lattices (17, 18). Previous experiments have shown that spin-spin interactions between neighboring atoms can be implemented in discrete time steps (19, 20) by bringing the atoms together on a single site and carrying out controlled collisions (20–22) or on-site exchange interactions (23). The superexchange interactions demonstrated here, however, directly implement nearest-neighbor spin interactions in the many-body system and allow for a continuous “analog” simulation of spin lattice Hamiltonians.

We probe the superexchange interactions by first preparing two atomic spin states of ⁸⁷Rb in an antiferromagnetic order (24) and then recording the time evolution of the spins of neighboring atoms in isolated double-well potentials (25–27) for weak to strong tunnel couplings. For dominating on-site interactions over the tunnel coupling between lattice sites, we find pronounced sinusoidal spin oscillations due to an effective Heisenberg-type superexchange Hamiltonian, whereas for stronger tunnel coupling, a more complex dynamics emerges. In addition, we show how the strength and sign of the superexchange interaction can be directly controlled by introducing a potential bias between neighboring wells. Furthermore, we find that corrections to the two-site Bose-Hubbard model (BHM) that take into account the direct interaction between particles on neighboring lattice sites are needed to fully explain our data.

Theoretical model. An isolated system of two coupled potential wells constitutes the simplest concept for the investigation of superexchange-mediated spin dynamics between neighboring atoms. We consider a single double-well potential occupied by a pair of bosonic atoms with two different spin states denoted by $|\uparrow\rangle$ and $|\downarrow\rangle$. If the vibrational level splitting in each well is much larger than all other relevant energy scales and intersite interactions are neglected, the system can be described in a two-mode approximation by a two-site version of the Bose-Hubbard Hamiltonian

$$\hat{H} = \sum_{\sigma=\uparrow,\downarrow} \left[-J(\hat{a}_{\sigma L}^\dagger \hat{a}_{\sigma R} + \hat{a}_{\sigma R}^\dagger \hat{a}_{\sigma L}) - \frac{1}{2} \Delta(\hat{n}_{\sigma L} - \hat{n}_{\sigma R}) \right] + U(\hat{n}_{\uparrow L} \hat{n}_{\downarrow L} + \hat{n}_{\uparrow R} \hat{n}_{\downarrow R}) \quad (1)$$

where the operators $\hat{a}_{\sigma L,R}^\dagger$ and $\hat{a}_{\sigma L,R}$ create and annihilate an atom with spin σ in the left and right well respectively, $\hat{n}_{\sigma L,R}$ count the number of atoms per spin state and well, J is the tunnel matrix element, Δ is the potential bias or tilt along the double-well axis, and $U = U_{\uparrow\downarrow} = g \times \int W_{L,R}^4(\mathbf{x}) d^3x$ is the on-site interaction energy between two

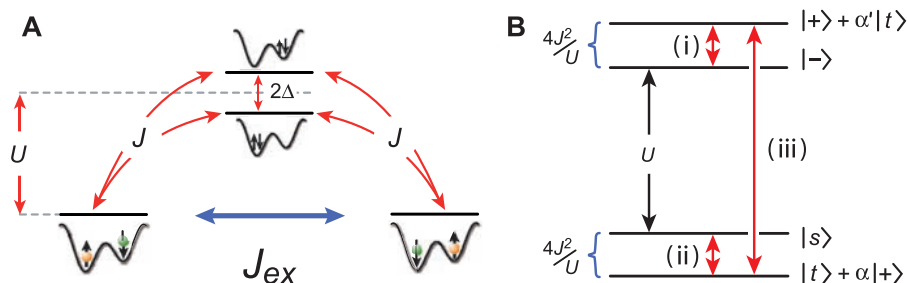


Fig. 1. Schematics of superexchange interactions. **(A)** Second-order hopping via $|\uparrow\downarrow,0\rangle$ and $|0,\uparrow\downarrow\rangle$ mediates the spin-spin interactions between atoms on different sides of the double well. **(B)** Energy levels for $\Delta = 0$ and $U \gg J$. The evolution in the upper doublet of states (i) corresponds to the correlated tunneling of atom pairs (27), whereas the superexchange takes place in the lower one (ii). Both doublets are coupled by first-order tunneling processes (iii).

¹Institut für Physik, Johannes Gutenberg-Universität, 55099 Mainz, Germany. ²Fachbereich Physik, Technische Universität Kaiserslautern, 67663 Kaiserslautern, Germany. ³Institute for Theoretical Atomic, Molecular and Optical Physics, Harvard-Smithsonian Center of Astrophysics, Cambridge, MA 02138, USA. ⁴Department of Physics, Boston University, Boston, MA 02215, USA. ⁵Physics Department, Harvard University, Cambridge, MA 02138, USA.

*These authors contributed equally to this work.

†To whom correspondence should be addressed. E-mail: bloch@uni-mainz.de

atoms in $|\uparrow\rangle$ and $|\downarrow\rangle$. Here, $g = (4\pi\hbar^2 a_s^{\uparrow\downarrow})/M$ is the effective interaction strength with $a_s^{\uparrow\downarrow}$ being the positive scattering length for the spin states used in the experiment, M is the mass of a single atom, and $w_{L,R}(\mathbf{x})$ denote the wave functions for a particle localized on the left or right side of the double well. The state of the system can be described as a superposition of the Fock states $\{|\uparrow,\downarrow\rangle, |\downarrow,\uparrow\rangle, |\uparrow\downarrow,0\rangle, |0,\uparrow\downarrow\rangle\}$, where the left and right side in the notation represent the occupation of the left and right well, respectively, and the states $|\uparrow\downarrow,0\rangle$ and $|0,\uparrow\downarrow\rangle$ are spin triplet states. In the following, we will focus on the dynamical evolution of the population imbalance $x = n_L - n_R$ and the Néel order parameter or “spin imbalance” $N_z = (n_{\uparrow L} + n_{\uparrow R} - n_{\downarrow R} - n_{\downarrow L})/2$ starting with double wells initially prepared in $|\uparrow,\downarrow\rangle$. Here, $n_{\uparrow,\downarrow,L,R} = \langle \hat{n}_{\uparrow,\downarrow,L,R} \rangle$ denote the corresponding quantum mechanical expectation values and $n_{L,R} = n_{\uparrow L,R} + n_{\downarrow L,R}$.

In the limit of dominating interactions ($U \gg J$), when starting in the subspace of singly occupied wells spanned by $|\uparrow,\downarrow\rangle$ and $|\downarrow,\uparrow\rangle$, the energetically high-lying states $|\uparrow\downarrow,0\rangle$ and $|0,\uparrow\downarrow\rangle$ can only be reached as “virtual” intermediate states in second-order tunneling processes. Such processes lead to a nonlocal (super) spin-exchange interaction, which couples the states $|\uparrow,\downarrow\rangle$ and $|\downarrow,\uparrow\rangle$ (Fig. 1A). More generally, for an arbitrary spin configuration with equal interaction energies $U_{\uparrow\uparrow} = U_{\downarrow\downarrow} = U_{\uparrow\downarrow}$ (28), the second-order hopping events are described by an isotropic Heisenberg-type effective spin Hamiltonian in the limit $U \gg J$ (3, 15, 29, 30):

$$\hat{H}_{\text{eff}} = -2J_{\text{ex}} \hat{S}_L \cdot \hat{S}_R \\ = -J_{\text{ex}} (\hat{S}_L^+ \hat{S}_R^- + \hat{S}_L^- \hat{S}_R^+) - 2J_{\text{ex}} \hat{S}_L^z \hat{S}_R^z \quad (2)$$

where $\hat{S}_{L,R}^{\pm} = |\uparrow\rangle\langle\downarrow|_{L,R} + |\downarrow\rangle\langle\uparrow|_{L,R}$ and $\hat{S}_{L,R}^z = (\hat{n}_{\uparrow L,R} - \hat{n}_{\downarrow L,R})/2$ denote the corresponding spin operators of the system, with $\hat{S}_{L,R}^{\pm} = \hat{S}_x \pm i\hat{S}_y$. The effective coupling strength J_{ex} represents the superexchange and can readily be evaluated by perturbation theory up to quadratic order in the tunneling operator, which yields $J_{\text{ex}} = 2J^2/U$.

When a potential bias $\Delta > 0$ is applied, the degeneracy of the two intermediate states in the superexchange process is lifted (Fig. 1A). For $J, \Delta \ll U$ this leads to a modification of the effective superexchange coupling with now $J_{\text{ex}} = J^2/(U + \Delta) + J^2/(U - \Delta) = 2J^2U/(U^2 - \Delta^2)$ (15). By tuning the bias to $\Delta > U$, it is possible to change the sign of J_{ex} and therefore to switch between ferromagnetic and antiferromagnetic superexchange interactions. For $J \ll |U - \Delta|$, the picture of an effective coupling via two virtual intermediate states is again valid, and the full reversal to $J_{\text{ex}} = -2J^2/U$ is found to be reached for $\Delta = \sqrt{2}U$.

For symmetric double wells ($\Delta = 0$), the Hamiltonian Eq. 1 can be diagonalized analytically to give a valid picture for all values of J and U within the single-band BHM. A convenient basis is given by the spin triplet and singlet state $|t/s\rangle = (|\uparrow,\downarrow\rangle \pm |\downarrow,\uparrow\rangle)/\sqrt{2}$ and the states $|\pm\rangle \equiv$

$(|\uparrow\downarrow,0\rangle \pm |0,\uparrow\downarrow\rangle)/\sqrt{2}$. Two of the eigenstates are linear combinations of $|t\rangle$ and $|\pm\rangle$, where the one having the larger overlap with $|t\rangle$ is the ground state. The spin singlet $|s\rangle$ and the state $|\mp\rangle$ are already eigenstates themselves with energy 0 and U , respectively (Fig. 1B). As a direct consequence, $|\mp\rangle$ cannot be reached from the initial state $|\uparrow,\downarrow\rangle = (|s\rangle + |t\rangle)/\sqrt{2}$. Therefore, the dynamical evolution of the spin imbalance contains only two frequencies

$$\hbar\omega_{1,2} = \frac{U}{2} \left(\sqrt{\left(\frac{4J}{U}\right)^2 + 1} \pm 1 \right) \quad (3)$$

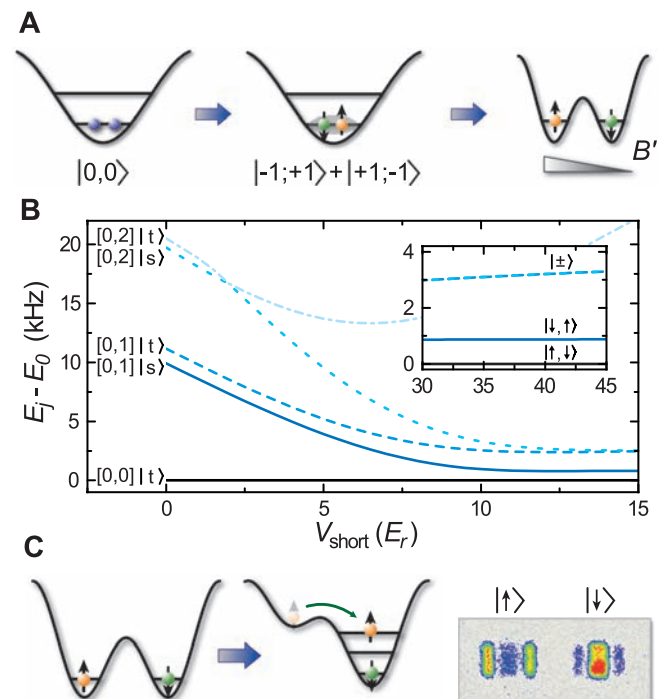
The extraction of these frequencies from time-resolved measurements allows for the determination of $2J = \hbar\sqrt{\omega_1\omega_2}$ and $U = \hbar(\omega_1 - \omega_2)$ within the BHM.

Because these frequencies can be measured with high accuracy, we are able to observe deviations from the simple BHM. We obtain a first correction by the inclusion of nearest-neighbor interactions (3) in an extended two-site Bose-Hubbard model [EBHM; see Eq. S1 in (31)]. This modification introduces the interwell interaction energy $U_{LR} = g \times \int w_L^2(\mathbf{x})w_R^2(\mathbf{x})d^3x$ and a correction to the tunneling matrix element, which becomes $J' = J + \Delta J$, where $\Delta J = -g \times \int w_L^3(\mathbf{x})w_R(\mathbf{x})d^3x$. The interwell interaction leads to a direct spin-exchange term, which in the limit $U \gg J$ reduces the corrected superexchange coupling to $J_{\text{ex}} = 2J'^2/U - U_{LR}$. Although we find that the corrections to the pure two-site BHM are not negligible in the experimentally relevant parameter region, numerical

calculations based on the multiband Schrödinger equation show that the direct exchange can never overcome the superexchange coupling term (fig. S1) and therefore change the nature of the ground state to be antiferromagnetic. This is in agreement with the Lieb-Mattis theorem (32), which states that the ground state for two bosons has to be a spin-triplet state.

Initial state preparation. To investigate the spin dynamics between neighboring atoms, we initially prepare a sample of ultracold neutral atoms with two relevant internal states $|\uparrow\rangle$ and $|\downarrow\rangle$ in a three-dimensional (3D) array of double wells with Néel-type antiferromagnetic order $|\uparrow\downarrow\uparrow\downarrow\uparrow\downarrow\dots\rangle$ along one spatial direction (Fig. 2A). State preparation was started by loading a ^{87}Rb Bose-Einstein condensate of typically $\sim 8 \times 10^4$ atoms in the $|F = 1, m_F = -1\rangle$ Zeeman sublevel with no discernible thermal fraction from a magnetic trap with high offset field into a 3D optical lattice of double-well potentials (25). This “superlattice” potential is obtained by superimposing on one axis two standing light fields with periodicity 382.5 nm (short lattice) and 765 nm (long lattice) and additional standing waves with periodicity 420 nm on the two perpendicular axes (27). Controlling all depths and the relative phase of the short and long lattice allows one to tune the double-well configuration in terms of the Hamiltonian parameters J, U , and Δ . The depths of the lattices are given in units of the short-lattice recoil energy $E_r = \hbar^2/(2M\lambda^2)$ with $\lambda = 765$ nm throughout the article. The loading ramps were optimized to favor an occupation of two atoms per double well and to avoid heating to higher vibrational levels (31). After merging the double wells by

Fig. 2. State preparation and detection. **(A)** Spin triplet pairs are created on doubly occupied lattice sites and subsequently split under the influence of a magnetic field gradient B' to obtain antiferromagnetic Néel order. **(B)** Evolution of the eigenenergies with respect to the ground-state energy during the splitting with $V_{\text{long}} = 10 E_r$, $V_{\text{trans}} = 25 E_r$, and a gradient of $B' = 17$ G/cm. The notation $[v_1, v_2]$ denotes the number of vibrational excitations for the first and second particle. The inset shows the eigenenergies and (eigen)-states for the final barrier height of $V_{\text{short}} = 44 E_r$. **(C)** Detection of the population and spin imbalance. The population of the left well is transferred to a higher vibrational level of the underlying long-lattice well (25, 27). Subsequent band mapping and a Stern-Gerlach filter allow one to determine $x(t)$ and $N_z(t)$ from the time-of-flight images.



ramping down the short lattice, a microwave rapid adiabatic passage was used to transfer all atoms into the $|F = 1, m_F = 0\rangle$ state. Subsequently, the magnetic trap is switched off and while maintaining a homogeneous offset field of ~ 1.2 G, atom pairs were coherently transferred from $|m_F = 0; m_F = 0\rangle$ into spin triplet pairs $(|+1; -1\rangle + |1; +1\rangle)/\sqrt{2}$ by means of spin-changing collisions (33, 34). The two magnetic sublevels $|m_F = \pm 1\rangle$ correspond to the two spin states $|\uparrow\rangle$ and $|\downarrow\rangle$. The remaining atoms in the $|m_F = 0\rangle$ state, e.g., on singly occupied sites, are transferred into $|F = 2, m_F = 0\rangle$ and removed in a filtering sequence before the detection (31).

Finally, the short lattice was ramped up slowly in 20 ms, thereby inhibiting a coherent splitting of the atom pairs and leaving the double wells in a state with one atom on each side (26). For the time of the ramping up, a magnetic field gradient of $B' \approx 17$ G/cm in the direction of the superlattice is switched on. Therefore, the degeneracy of the states $|\uparrow, \downarrow\rangle$ and $|\downarrow, \uparrow\rangle$ in the double well is lifted by ~ 900 Hz, which enables an adiabatic loading of the state $|\uparrow, \downarrow\rangle$ during the splitting process (Fig. 2B). Numerical integration of a multiband ansatz for this procedure yields an expected fidelity of $>99\%$ for creating an antiferromagnetic order along the axis of the superlattice. The mean population imbalance $x(t)$ and spin imbalance $N_z(t)$ of the ensemble of double wells was detected by applying a mapping technique (26, 27) combined with a Stern-Gerlach filter (Fig. 2C). A maximum spin imbalance of 60 to 70% was observed for our initial state corresponding to a probability of 80 to 85% for having prepared the desired state $|\uparrow, \downarrow\rangle$. We believe that this measured value is mainly reduced as a result of our detection method. Direct spin-exchange processes emerge during the mapping sequence (23) and can lead to a mixing of the spin configuration and thus a reduction of the measured Néel order parameter (31).

Time-resolved observation of superexchange interactions. The spin dynamics are initiated by rapidly ramping down the short lattice and thereby the double-well barrier in 200 μs , thus substantially increasing the tunneling and superexchange couplings. After letting the system evolve for a hold time t , the spin configuration was frozen out by ramping up the barrier in 200 μs , quenching both J and J_{ex} again. The measurement of the ensemble averages $x(t)$ and $N_z(t)$ is carried out as described above.

Three typical time traces obtained by this procedure are shown in Fig. 3. For low barrier depths ($J/U > 1$), we observe a pronounced time evolution of the spin imbalance $N_z(t)$ consisting of two frequency components with comparable amplitudes and frequencies (Fig. 3A). With increasing interaction energy U relative to J , the frequency ratio increases, leaving a slow component with almost full amplitude and an additional high-frequency modulation with small amplitude (Fig. 3B). The fast component corresponds to first-order tunneling due to the coupling of $|t\rangle$ and $|+\rangle$, which becomes more and more off-resonant as the barrier height is increased and therefore J/U is decreased. For $J/U \ll 1$, it is completely suppressed, and the only process visible is the superexchange oscillation (Fig. 3C). For all barrier heights, the population imbalance $x(t)$ stays flat, emphasizing that even though strong spin currents are present in the system, no net mass flow can be observed for our initial state. We fit the traces for $N_z(t)$ with a sum of two damped sine waves with variable frequencies $\omega_{1,2}/2\pi$ and amplitudes $A_{1,2}$. For the damping we assume Gaussian characteristics with $1/e$ -damping constants $\gamma_{1,2}$. The results of the fit are displayed in Fig. 4. For $V_{\text{short}} \geq 15 E_r$ (Fig. 4A, inset), we can identify only a single frequency component corresponding to the superexchange oscillation with $4J^2/\hbar U$ and full relative amplitude (Fig. 4B). We are able to observe this frequency down to 4.8(4) Hz at

$J/U = 0.023$ for $V_{\text{short}} = 20 E_r$. The damping of the signal can be explained by the inhomogeneous distribution of coupling parameters due to the Gaussian shape of the lattice beams, which leads to a dephasing of the evolution within the ensemble. For $V_{\text{short}} \geq 17 E_r$, additional damping mechanisms like tunneling to empty adjacent lattice sites (defects) or small residual inhomogeneous magnetic field gradients become relevant and limit the measurements (Fig. 4C).

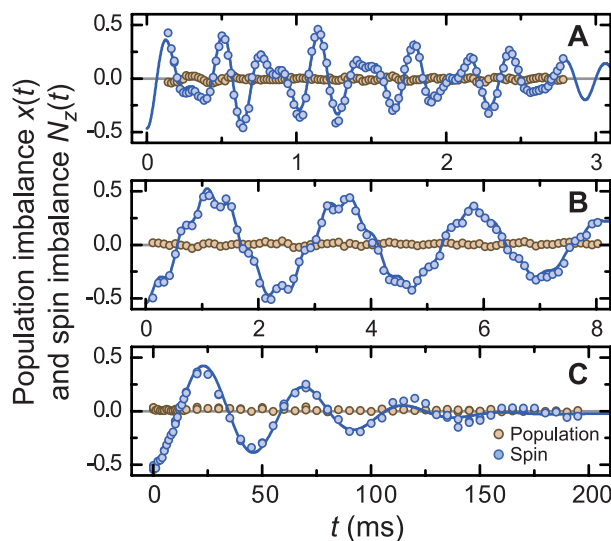
The comparison of the results with the theoretical predictions by the simple BHM shows statistically significant deviations at low barrier heights, which cannot be explained by our uncertainties in the lattice depths. In this region, the EBHM can model the experimental data much more accurately. This can be understood by the fact that the interwell interaction energy increases with decreasing barrier and begins to noticeably influence the dynamics (31). In fact, the EBHM description yields $\hbar(\omega_1 - \omega_2) = U + 3U_{\text{LR}}$ and therefore directly explains the upward trend of this frequency difference for small short-lattice depths (fig. S2). For large barrier heights, our experimental data are compatible with both models within the uncertainties of the lattice depths. However, here the predictions of the EBHM are always closer to the measured values.

Sign reversal of the effective coupling parameter. To demonstrate the controllability of superexchange interactions, we investigated the spin dynamics with an applied bias on the double wells for a short lattice depth of $15 E_r$ and the same depths for the long and transverse lattice as before. Starting with an initial antiferromagnetically ordered state, as above, we first let the system evolve in symmetric double wells ($\Delta = 0$) for $t_0 = 4.5$ ms until the first node $N_z(t) = 0$ of the spin imbalance is reached for the state $(|t\rangle + |s\rangle)/\sqrt{2}$ (Fig. 5). After freezing out the relative phase between $|s\rangle$ and $|t\rangle$ by ramping up the potential barrier, a defined potential bias Δ is applied and a second evolution sequence with hold time $t' = t - t_0$ is initialized by ramping down the short lattice again to $15 E_r$. The subsequent detection follows the scheme described above.

Figure 5A shows the evolution of the spin imbalance $N_z(t)$ in symmetric double wells together with the time traces for two different bias energies $\Delta > U$, yielding an effective coupling of $J_{\text{ex}}(\Delta) \approx -J_{\text{ex}}(\Delta = 0)$ and $-J_{\text{ex}}(\Delta = 0)/2$, respectively. The sign reversal of J_{ex} due to the introduction of the bias is directly visible by the change in slope of the spin imbalance $t = t_0$. It should be noted that the now negative sign of J_{ex} for bosons does not imply a violation of the Lieb-Mattis theorem, because the new ground state in this regime is the spin triplet state $|\uparrow\downarrow, 0\rangle$ and the superexchange couples the first and second excited states $|s\rangle$ and $|t\rangle$, which have reversed order for $\Delta > U$ (Fig. 5B, left inset).

The introduction of a nonzero tilt leads to an increased sensitivity of the exchange frequency to fluctuations due to the inhomogeneities in the

Fig. 3. Spin and population dynamics in symmetric double wells. The time evolution of the mean spin $N_z(t)$ (blue circles) and population imbalance $x(t)$ (brown circles) are shown for three barrier depths within the double-well potential: (A) $V_{\text{short}} = 6 E_r$, $J/U = 1.25$; (B) $V_{\text{short}} = 11 E_r$, $J/U = 0.26$; and (C) $V_{\text{short}} = 17 E_r$, $J/U = 0.048$. The measured traces for the spin imbalance are fitted with the sum of two damped sine waves (blue lines). The population imbalance $x(t)$ stays flat for all traces.



array of double wells, which are most effective around $\Delta \approx U$. Therefore, the damping of the signal due to dephasing is stronger as Δ approaches U . A fit of a single dampened sine

wave to the time traces obtained for various tilts yields the frequency curve shown in Fig. 5B together with the amplitude of the oscillation. Starting around 50 Hz, the oscillation frequency

reaches a resonance for $\Delta/U \approx 1$, where the amplitude reverses sign, leading to the observed time reversal in the dynamics.

Summary and outlook. We have demonstrated time-resolved measurements of superexchange spin interactions between ultracold atoms on neighboring lattice sites and have shown how to control such interactions with optical superlattices. Comparing the measurements to theoretical predictions of these spin interactions from first principles, we find excellent agreement of our data to an extended two-site version of the BHM. Although superexchange interactions become exponentially suppressed for deep optical lattices, the coupling strength $2J_{ex}/h$ can be several hundred hertz for lattice depths of around 12 to $15 E_r$ and thus almost a factor of 1000 larger than the direct magnetic dipole-dipole interaction of Rb atoms on neighboring lattice sites. Coupling strengths one order of magnitude larger than the ones shown here, however, could still be achieved with the use of electric dipole-dipole-mediated spin interactions between ground-state polar molecules (35).

The demonstrated scheme to change the superexchange coupling strength and reverse the sign of the spin interaction can also be applied to the full 1D chain, offering new possibilities for engineering spin-spin interactions in optical lattices. It is now, e.g., conceivable to engineer a setup with ferromagnetic interactions along one and antiferromagnetic interactions along another lattice direction. Furthermore, one can dynamically switch between ferro- and antiferromagnetic interactions along a given lattice direction and follow the subsequent dynamical evolution of the quantum spin system.

When the presented loading scheme is carried out without any magnetic gradient field during the splitting process, a valence-bond solid (VBS) type spin state (3, 36) can be efficiently engineered. Such VBS states can be viewed as a large array of robust Bell pairs (37, 38). In principle, the superexchange interaction can be changed to be of Ising type, e.g., by tuning the interspecies scattering length (15). Thereby, it can be used to create large entangled states out of the initially disconnected pairs, which have been shown to be powerful resources for measurement-based quantum computation (13, 39). Moreover, controlling the superexchange interactions along different lattice directions also offers novel possibilities for the generation of topological many-body states for quantum information processing (14, 15).

References and Notes

1. E. Ising, *Z. Phys. A* **31**, 253 (1925).
2. W. Heisenberg, *Z. Phys. A* **38**, 411 (1926).
3. A. Auerbach, *Interacting Electrons and Quantum Magnetism* (Springer, Berlin, 2006).
4. P. A. M. Dirac, *Proc. R. Soc. London Ser. A* **112**, 661 (1926).
5. P. A. M. Dirac, *Proc. R. Soc. London Ser. A* **123**, 714 (1929).
6. W. Heisenberg, *Z. Phys.* **49**, 619 (1928).
7. H. A. Kramers, *Physica* **1**, 182 (1934).
8. P. Anderson, *Phys. Rev.* **79**, 350 (1950).

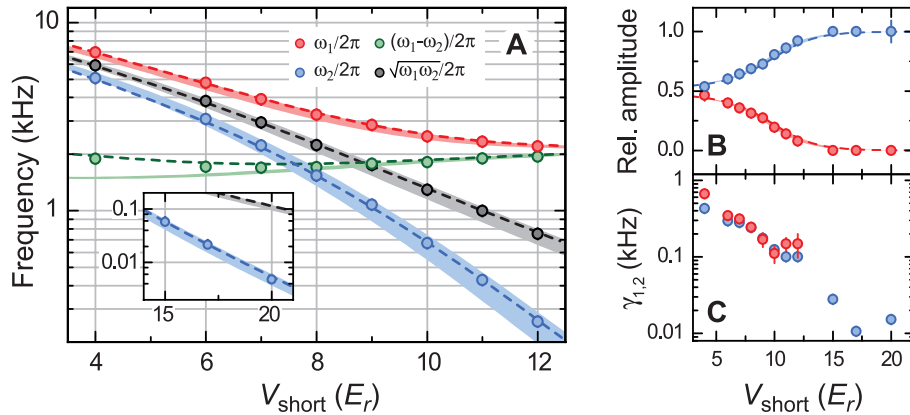
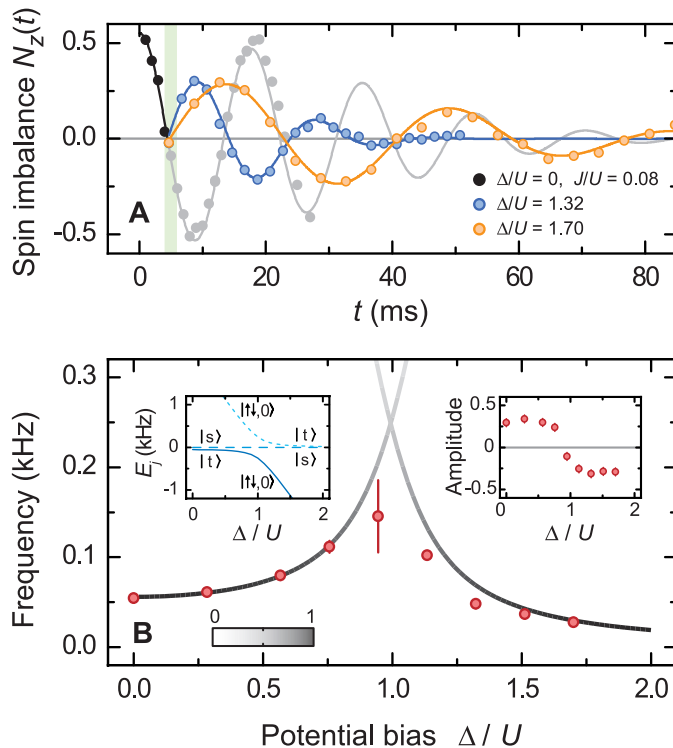


Fig. 4. Frequency components of the spin oscillations. **(A)** The frequencies obtained by fitting the spin imbalance data for various values of V_{short} (red and blue circles), as well as the frequency difference and the geometrical mean (green and black circles), are compared to the theoretical predictions of the simple BHM (colored regions). The width of the regions represents a 2% uncertainty in all lattice depths. The 2σ error bars on the fit results and extracted values are in all cases smaller than the data points. The dashed lines are the predictions of the EBHM. The inset shows the data for high barriers, where only a single frequency component can be identified. **(B)** The plot of relative amplitudes versus short lattice depth shows the suppression of the first-order tunneling process toward small values of J/U . The damping coefficients for the two oscillatory components versus lattice depth are displayed in **(C)**. The error bars denote the 2σ uncertainties as obtained from the fit results.

Fig. 5. Sign reversal of the superexchange coupling. **(A)** After a quarter of a superexchange oscillation in symmetric double wells (black and gray dots, $J/U = 0.08$), a defined bias is applied, leading to a reversal in the slope of the spin imbalance and ongoing oscillations. For $\Delta/U = 1.32$ (blue circles), the magnitude of the coupling is almost the same as for $\Delta = 0$, whereas it is decreased to $\sim 50\%$ for $\Delta/U = 1.70$ (orange circles). **(B)** The fit of the data for various tilts to a damped sine yields a resonance in frequency at $\Delta \approx U$, where the amplitude reverses sign (right inset). The solid lines show the theoretically expected frequencies for the given parameters where the shading reflects the amplitude of the corresponding Fourier component. The left inset shows the three lowest eigenenergies of the Bose-Hubbard Hamiltonian versus the potential bias. The error bars denote the 2σ uncertainties as obtained from the fit results.



9. P. Lee, N. Nagaosa, X.-G. Wen, *Rev. Mod. Phys.* **78**, 17 (2006).
10. G. Burkard, D. Loss, D. P. DiVincenzo, *Phys. Rev. B* **59**, 2070 (1999).
11. J. R. Petta *et al.*, *Science* **309**, 2180 (2005).
12. A. M. Rey, V. Gritsev, I. Bloch, E. Demler, M. D. Lukin, *Phys. Rev. Lett.* **99**, 140601 (2007).
13. H. J. Briegel, R. Raussendorf, *Phys. Rev. Lett.* **86**, 910 (2001).
14. A. Kitaev, *Ann. Phys.* **321**, 2 (2006).
15. L.-M. Duan, E. Demler, M. D. Lukin, *Phys. Rev. Lett.* **91**, 090402 (2003).
16. L. Santos *et al.*, *Phys. Rev. Lett.* **93**, 030601 (2004).
17. M. Lewenstein *et al.*, *Adv. Phys.* **56**, 243 (2007).
18. K. Eckert, L. Zawitkowski, M. J. Leskinen, A. Sanpera, M. Lewenstein, *N. J. Phys.* **9**, 1 (2007).
19. E. Jané, G. Vidal, W. Dür, P. Zoller, J. Cirac, *Quantum Inf. Comput.* **3**, 15 (2003).
20. A. Sørensen, K. Mølmer, *Phys. Rev. Lett.* **83**, 2274 (1999).
21. D. Jaksch, H. J. Briegel, J. I. Cirac, C. W. Gardiner, P. Zoller, *Phys. Rev. Lett.* **82**, 1975 (1999).
22. O. Mandel *et al.*, *Nature* **425**, 937 (2003).
23. M. Anderlini *et al.*, *Nature* **448**, 452 (2007).
24. L. Néel, *Ann. Phys. IIe Ser.* **5**, 232 (1936).
25. J. Sebby-Strabley, M. Anderlini, P. Jessen, J. Porto, *Phys. Rev. A* **73**, 033605 (2006).
26. J. Sebby-Strabley *et al.*, *Phys. Rev. Lett.* **98**, 200405 (2007).
27. S. Fölling *et al.*, *Nature* **448**, 1029 (2007).
28. For the spin states used in our experiment, the interaction energies for the different intercombinations of spins vary by only a few percent.
29. A. B. Kuklov, B. V. Svistunov, *Phys. Rev. Lett.* **90**, 100401 (2003).
30. E. Altman, W. Hofstetter, E. Demler, M. D. Lukin, *N. J. Phys.* **5**, 113 (2003).
31. Materials and methods are available as supporting material on Science Online.
32. E. Lieb, D. Mattis, *Phys. Rev.* **125**, 164 (1962).
33. A. Widera *et al.*, *Phys. Rev. Lett.* **95**, 190405 (2005).
34. F. Gerbier, A. Widera, S. Fölling, O. Mandel, I. Bloch, *Phys. Rev. A* **73**, 041602(R) (2006).
35. A. Micheli, G. K. Brennen, P. Zoller, *Nat. Phys.* **2**, 341 (2006).
36. F. Alet, A. M. Walczak, M. P. A. Fisher, *Physica A* **369**, 122 (2006).
37. C. F. Roos *et al.*, *Phys. Rev. Lett.* **92**, 220402 (2004).
38. C. Langer *et al.*, *Phys. Rev. Lett.* **95**, 060502 (2005).
39. F. Verstraete, J. I. Cirac, *Phys. Rev. A* **70**, 060302(R) (2004).
40. We acknowledge helpful discussions with B. Paredes and funding by the Deutsche Forschungsgemeinschaft, the European Union (OLAQUI, SCALA), NSF, Air Force Office of Scientific Research (MURI, FA8655-07-1-3090), and the Packard Foundation. S.T. acknowledges financial support from the graduate class of excellence on materials with strong correlations (MATCOR).

Supporting Online Material

www.sciencemag.org/cgi/content/full/1150841/DC1
SOM Text

Figs. S1 and S2
References and Notes

21 September 2007; accepted 6 December 2007

Published online 20 December 2007;

10.1126/science.1150841

Include this information when citing this paper.

Natural Streams and the Legacy of Water-Powered Mills

Robert C. Walter*† and Dorothy J. Merritts*†

Gravel-bedded streams are thought to have a characteristic meandering form bordered by a self-formed, fine-grained floodplain. This ideal guides a multibillion-dollar stream restoration industry. We have mapped and dated many of the deposits along mid-Atlantic streams that formed the basis for this widely accepted model. These data, as well as historical maps and records, show instead that before European settlement, the streams were small anabranching channels within extensive vegetated wetlands that accumulated little sediment but stored substantial organic carbon. Subsequently, 1 to 5 meters of slackwater sedimentation, behind tens of thousands of 17th- to 19th-century milldams, buried the presettlement wetlands with fine sediment. These findings show that most floodplains along mid-Atlantic streams are actually fill terraces, and historically incised channels are not natural archetypes for meandering streams.

The meandering gravel-bedded stream bordered by a self-formed, fine-grained floodplain emerged as the characteristic river form based on pioneering studies in mid-Atlantic and western streams of the United States (1–4). Today, this ideal—of alternating pools and riffles along sinuous channels with gravel point bars and fine-grained overbank floodplain deposits—guides a multibillion-dollar stream restoration industry (5, 6). Many streams in the low-relief, tectonically inactive mid-Atlantic Piedmont of the United States are deeply incised, with steep eroding banks, and carry anomalously high amounts of suspended sediment (7). Fine-grained deposits bordering many eastern streams are thicker than would be expected from just their recent flood deposits (1, 3). These Holocene deposits typically form broad surfaces, referred to as the “valley

flat,” that were interpreted as floodplains formed by a combination of migrating, meandering stream channels and overbank deposition of silts and clays (1, 3, 8). The geometry of single-channel meandering streams has been viewed as the result of self-adjusting hydraulic variables in response to changing discharge and sediment load, and agriculture and urbanization have been cited widely as the causes of recent aggradation and degradation (1, 3, 4, 8–10). This pattern of stream development and morphology has been considered as typical of streams and rivers in stable landscapes.

We observe that crests of breached, historic milldams merge with valley-flat surfaces and that most modern streams are incised deeply below this surface. This observation led us to hypothesize that a rapid, regional transformation of stream valleys had occurred in eastern North America, from widespread aggradation as a result of damming (base-level rise) to subsequent incision and bank erosion due to dam breaching (base-level fall). We propose that valley sedimentation not only resulted from accelerated hillslope erosion caused by deforestation and agricultural

development (8, 11) but also was coupled with widespread valley-bottom damming for water power, after European settlement, from the late 17th century through the early 20th century. Damming was essential to the extensive trapping of sediment in broad valley flats that correspond to reservoir surfaces.

We test this hypothesis by examining the following lines of evidence: (i) historical accounts of widespread, intensive water-powered milling that impacted most first- to third-order streams in the mid-Atlantic region; (ii) historical maps showing multiple dams and ponds, and our observations in the field and from light detection and ranging (LIDAR) data of aggradation in these ponds that caused sedimentation upstream into tributaries and swales; (iii) historical, geological, and geochemical data showing rapid sedimentation in valley bottoms during the period of early land clearing; (iv) field observations and remote-sensing data, including LIDAR, showing that downstream-thickening wedges of sediment grade to milldam heights and, hence, that dams produced temporary, higher base levels; and (v) field observations and laboratory data showing that the morphologies and functions of presettlement streams were substantially different from those of modern streams. We revisited the same streams and specific reaches used in early studies that pioneered modern fluvial geomorphology, including fundamental ideas regarding meander migration, floodplain formation, hydraulic geometry, and fluvial response to land clearing. These streams include the Brandywine River (in Pennsylvania and Delaware) and Seneca Creek, Watts Branch, and Western Run (in Maryland) (1–4, 8, 9, 11), all of which lie within the Piedmont physiographic province of the mid-Atlantic region. In all, we studied Piedmont streams in 20 watersheds throughout Pennsylvania and Maryland (drainage areas from 11 to 1230 km²; fig. S1).

Milldam history. Dam building for water power in the eastern United States began in the

Department of Earth and Environment, Franklin and Marshall College, Post Office Box 3003, Lancaster, PA 17604–3003, USA.

*These authors contributed equally to this work.

†To whom correspondence should be addressed. E-mail: robert.walter@fandm.edu (R.C.W.); dorothy.merritts@fandm.edu (D.J.M.)